ACS APPLIED MATERIALS & INTERFACES

Research Article

www.acsami.org

Shape-Selective Oriented Cerium Oxide Nanocrystals Permit Assessment of the Effect of the Exposed Facets on Catalytic Activity and Oxygen Storage Capacity

Thadathil S. Sreeremya,[†] Asha Krishnan,[†] Kottayilpadi C. Remani,[†] Kashinath R. Patil,[‡] Dermot F. Brougham,[§] and Swapankumar Ghosh*[,†,▽]

[†]Functional Materials Section (MSTD), National Institute for Interdisciplinary Science & Technology (NIIST), Council of Scientific & Industrial Research (CSIR), Trivandrum−695019, India

[‡]National Chemical Laboratory, Pune, India

[§]National Institute for Cellular Biotechnology, School of Chemical Sciences, Dublin City University, Glasnevin, Dublin 9, Ireland

[▽]Presently working at ACTC Division, Central Glass & Ceramic Research Institute, CSIR, 196 Raja S. C. Mullick Road, Kolkata−700 032, India

Supporting Information

ABSTRACT: The catalytic performance of a range of nanocrystalline CeO_2 samples, prepared to have different morphologies, was measured using two accepted indicators; oxygen storage and diesel soot combustion. The same powders were characterized in detail by HR-TEM, XRD, XPS, and Raman methods. The study demonstrates that activity is determined by the relative fraction of the active crystallographic planes, not by the specific surface area of the powders. The physical study is a step toward quantitative evaluation of the relative contribution to activity of the different facets. The synthetic protocol permits fabrication of CeO_2 nanostructures with preferentially grown active planes, and therefore has potential in developing catalytic applications and in nanocompositing.

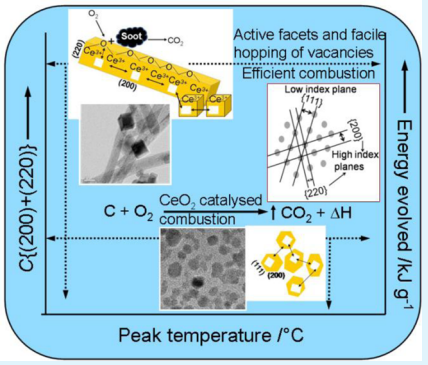

KEYWORDS: *ceria, nanocrystals, crystal facets, texture coefficient, chemical activities*

1. INTRODUCTION

Nanoscale cerium oxide crystals with the face-centered cubic (fcc) fluorite-type $Fm\bar{3}m$ crystal structure[1−4] have many properties that make them attractive materials for real applications; these include direct electrochemical oxidation of methane in solid oxide fuel cells,[5,6] in oxidation catalysis,[7,8] and as automobile exhaust catalysts.[9,10] This interest arises because of the redox activity of the Ce ions,[11,12] and because the physical and chemical properties can be tailored through doping or by varying grain size and shape.[13] Specifically, in catalytic applications of CeO_2, the crystallite size, the presence and number of oxygen vacancies, and the resulting lattice strain are critical to the performance of the materials.[14,15] The shape of CeO_2 nanocrystals is correlated with the predominance of particular crystal facets,[16,17] which exhibit different reactivities in various catalytic processes. Hence, methods that give control over crystal shape may provide a means to identify the key design aspects required to improve catalytic activity.

Anisotropic CeO_2 nanocrystals with rodlike[12,18] and cubelike[12] shapes exhibit higher CO conversion at lower temperature[18] and display higher oxygen storage capacity[12] than spheroidal particles, because of the presence of a greater proportion of {100} and {110} surfaces. Huang et al. observed strong morphology dependence of the CeO_2 support in catalytic performance of Pt/CeO_2 in CO oxidation, and they correlated the activities with the exposed crystal planes and the surface structure/morphologies of the CeO_2 support.[17] Similarly, it was recently reported that, for doped-CeO_2 nanocrystals, both H_2 selectivity and ethanol-reforming activity decrease in the order rod > tube > cube, compared to irregular nanoparticles with evenly distributed facets.[19] This was attributed to the combined effect of high surface area and exposed facets of {100}/{110} planes. On the other hand, Guan et al. reported conflicting observations that spherical particles, with relatively higher surface area, are more active in CO conversion than the rodlike and prism-shaped CeO_2 crystals.[20] Ravishankar et al. tested CeO_2/Pt nanohybrids as catalysts for the CO oxidation reaction. The availability of oxygen-deficient sites and the formation of the least stable carbonate species on the CeO_2 rods were ascribed as the reason for its high catalytic activity.[21] Fino et al. reported that nanostructured self-assembled CeO_2 stars possessing high

Received: January 11, 2015
Accepted: April 1, 2015
Published: April 1, 2015

DOI: 10.1021/acsami.5b00298
ACS Appl. Mater. Interfaces 2015, 7, 8545−8555

specific surface area (SSA), pore volume, and, as a result, high availability of contact points, showed improved performance in solid−solid catalysis.[22]

The apparent contradiction in these observations prompts the need for assessment of catalytic activity, not only in terms of crystal morphology but also in terms of the relative preponderance of the crystal facets. Among the low index facets of ceria (i.e., {111}, {100}, and {110}), the {100} facet is energetically unstable, transforming to {111} upon heating above 500 °C, and is catalytically more active than the other two planes.[23] However, the {110} surface has the lowest vacancy formation energy,[17,24−27] which is an observation that was first predicted by Conesa et al. on the basis of calculation.[28] The effect of the calcining[29] and deposition temperature[30] on preferred orientations of the different crystal facets in CeO_2 has been measured in terms of the changes in the texture coefficient and it was shown that temperature determines the kinetics of growth, as manifested in the smoothness of the grains, the crystallinity, the occurrence of preferential growth and the morphology. The texture coefficient of CeO_2 (200) reflection had a maximum of 6.7 at a laser power of 113 W and a deposition temperature of 836 K.[30] Fino et al. have evaluated the catalytic activity of ceria by combustion of carbon soot, although there was no detailed morphological or crystallographic assessment of the catalytic surfaces.[31] The consensus across the published literature is that CeO_2 crystals with a predominance of {100}/{110} planes over {111} planes are more catalytically active. However, to the best of our knowledge, there is no study correlating the chemical reactivity with the relative content of active crystal facets in CeO_2 crystals of different shapes and with quantitative analysis of Ce^{3+}.

Herein, we report simple synthetic methods for synthesizing cerium oxide nanocrystals of anisotropic shapes (nanorods and nanocubes), as well as crystals of spherical morphology. The nanopowders were characterized by X-ray diffraction (XRD), Fourier transform infrared spectroscopy (FT-IR), thermogravimetry, X-ray photoelectron spectroscopy (XPS), high-resolution transmission electron microscopy (HR-TEM), and Brunauer−Emmett−Teller (BET) surface area analysis. The abundance of exposed crystallographic planes was evaluated using the texture coefficient[32] for the three low-index planes in CeO_2 nanocrystals by performing Harris analysis[33] on XRD data, with supporting evidence provided by HR-TEM. The effect of size, shape, and BET surface area of fine CeO_2 nanocrystals on catalytic activity has been investigated by diesel soot combustion and temperature-programmed reduction (TPR) with H_2. Catalytic activity of CeO_2 crystals of different shapes and sizes have been explained in terms of texture coefficient of different crystal planes, this places understanding of the activity on a strong physical basis and identifies design goals for future catalyst development.

2. EXPERIMENTAL SECTION

Materials. The starting chemicals employed in the syntheses were $Ce(NO_3)_3{\cdot}6H_2O$ (>99.9%, Indian Rare Earths Ltd., India), and the precipitants were NaOH (analytical grade, Qualigens Fine Chemicals, India) and NH_4OH (25%, analytical grade, Qualigens Fine Chemicals, India). All the chemicals were used as received without further purification. All the chemical syntheses and washings were carried out using doubly distilled water obtained from a quartz glass distillation unit. A commercial ceria powder (CC) supplied by Kansal Enterprises (New Delhi, India) was also included in the present study for comparison.

Nanosized cerium oxides were synthesized by ammonia precipitation and precipitation using sodium hydroxide (NaOH), followed by hydrothermal treatment.

Ammonia Precipitation. Small crystals of cerium oxide were synthesized by ammonia precipitation using 0.05 M aqueous $Ce(NO_3)_3{\cdot}6H_2O$ (CN) solutions via the salt-into-precipitant (SIP) technique.[34] In a typical synthesis, CN solution (29 mmol) was added to 25% ammonia in a 2 L beaker so that the total volume of the reaction mixture was 580 mL. The net concentration of Ce ion was 50 mM, and the hydroxyl/cerium ratio (OH/Ce) in solution was greater than 10:1. The CN solution was added at a uniform rate over a period of 1 min under vigorous mechanical stirring, using a $^1/_8$ hp mechanical stirrer at ∼4000 rpm. The reaction was carried out at 30 °C (room temperature). A purple-colored precipitate formed within minutes after the addition of CN solution. The precipitate turned to yellow upon stirring further for ∼20 min, indicating the formation of cerium oxide (ceria). The stirring was continued for 3 h. The ceria precipitate was then collected by centrifugation and the excess ammonia was washed off with distilled water until the pH of the supernatant liquid was <8. The centrifuged mass was then washed twice with dry ethanol and dried in an air oven overnight at 65 °C; this is, henceforth, called AP.

Anisotropic CeO_2 by NaOH Precipitation Followed by One-Step Hydrothermal Treatment. *Cerium Oxide Nanorods.* In this case, a cerium nitrate precursor solution was prepared by dissolving CN (0.029 mol) in distilled water (100 mL). A precipitant solution was also prepared by dissolving NaOH (4.65 mol) in distilled water (481 mL). The two aqueous solutions were then mixed and stirred strongly for 30 min in a 2 L polypropylene beaker. On mixing, the net Ce-ion concentration was ∼50 mM. Subsequently, the milky reaction mixture was transferred into a 1 L Teflon lined autoclave vessel and the autoclave was sealed tightly. The precipitate was hydrothermally treated at 120 °C. After 24 h of hydrothermal treatment, the autoclave reactor was cooled and depressurized to room temperature naturally. The CeO_2 precipitate was then collected by centrifugation. The precipitate was washed with distilled water until the pH of the supernatant liquid was 7.5. The collected solid was then washed with ethanol twice. The washed precipitate was dried in an air oven at 65 °C overnight and, henceforth, will be called HT1 (hydrothermally treated at 120 °C/24 h). A fraction of this sample was subsequently annealed at 400 and 1000 °C for 4 h; the calcined samples will be called HT1C4 and HT1C1, respectively.

Cerium Oxide Nanocubes. Cerium oxide nanocubes were synthesized by autoclaving the freshly precipitated slurry at 180 °C, following a modified method described for synthesizing CeO_2 nanorods. Three modifications were introduced: (i) use of 5 M concentration of NaOH in the reaction mixture; (ii) lower hydroxyl/cerium ratio (OH/Ce) of 97:1, instead of 160:1; and (iii) the autoclaving temperature was increased from 120 °C to 180 °C. The final products were washed with distilled water until excess alkali was removed and dried at 65 °C. This product is denoted as HT2.

Cerium Oxide Nano-octahedra. Octahedral nanoparticles were synthesized via a reported procedure,[21,35] which involves hydrothermal treatment of an aqueous solution of CN (25 mmol) in the presence of trisodium phosphate (0.25 mmol) at

DOI: 10.1021/acsami.5b00298
ACS Appl. Mater. Interfaces 2015, 7, 8545−8555

170 °C for 12 h. The white precipitate was treated in similar way as in the case of cubes. This product is designated as HT3.

Catalytic Activity Tests. The reactivity of cerium oxide nanoparticles in catalyzing combustion of carbon was investigated by controlled combustion of a 40 mg mixture of CeO_2 catalyst, carbon soot (collected by burning diesel), and α-alumina using the TGA instrument. The rate of heating used in the ramp was 10 °C min^{-1} using standard α-alumina as reference in the temperature range of 50−800 °C. The sample for soot oxidation was prepared by mixing and grinding carbon, powdered CeO_2 and alumina powder (average particle size ∼450 nm, Condea Chemie, Germany) in the weight ratio 1:9:10 in an agate mortar. The inert alumina powder was added to prevent any thermal runaways. The catalytic activity evaluation was done on the prepared CeO_2 catalyst formulations. The total energy evolved was calculated for different CeO_2 powders from the thermal analysis profiles.

Temperature-Programmed Reduction in Hydrogen (H_2-TPR). Temperature-programmed reduction experiments were carried out using a 5% H_2−N_2 mixture (flow rate of 40 mL min^{-1}) at a heating rate of 10 °C min^{-1} with 0.1 g of CeO_2 up to 800 °C (upper temperature limit of the TPR equipment). The catalysts were heated at 120 °C for 2 h and cooled to room temperature in helium (40 mL min^{-1}) prior to the TPR experiment.

Characterization Techniques. The phase composition of the solid products were determined from the powder X-ray diffraction (XRD) patterns collected at room temperature using a Philips X'PERT PRO diffractometer with Ni-filtered Cu Kα_1 radiation (λ = 1.5406 Å). The X-ray data was collected on oven-dried powders in the 2θ range of 20°−100° at a scanning rate of 2° min^{-1} with a step size of 0.04°. Broadening of the XRD peaks (Bragg peaks) is related to the average grain size and microstrain in the crystal lattice originating from defects. Particle size information was obtained by analyzing the XRD peak widths using the Williamson-Hall (also known as Cauchy−Cauchy) procedure.[14,36] This is in preference to the Scherrer approach, which underestimates grain size when there is significant microstrain in the lattice.

The morphology and average size of the ceria nanoparticles were observed by TEM analysis carried out in an HR-TEM system (FEI Tecnai 30 G^2 S-Twin) operated at 300 kV. Samples for TEM study were prepared by dropping a micro droplet of suspension of nanopowder in isopropanol on to a 400 mesh carbon-coated copper grid and drying the excess solvent naturally. Raman spectra were taken using a HR800 LabRAM confocal Raman spectrometer having excitations by a 20 mW, 633 nm He−Ne laser. The spectrum was recorded using a Peltier cooled CCD detector with an acquisition time of 10 s using a 5× objective. Thermal studies of the powders were carried out using a Perkin−Elmer, Model STA 6000 simultaneous DTA-TGA system in ambient atmosphere heated at a constant rate of 10 °C min^{-1} under air purge. A blank run was carried out with alumina alone before any experiment for the baseline correction. X-ray photoelectron spectroscopy (XPS) spectra for nanosized CeO_2 powders were recorded on a VG Microtech Multilab ESCA 3000 spectrometer, maintaining a base pressure of the analysis chamber in the range of 3−6 × 10^{-10} Torr. Mg Kα (1253.6 eV) was used as the X-ray source. Selected spectra, especially N 1s and valence band spectra, were recorded to eliminate the overlap between different Auger and/or core levels. Binding energy (BE) calibration was performed with Au $4f_{7/2}$ core level at 83.9 eV. The XPS data was deconvoluted with XPSPEAK 4.1 software which produced stable and almost superimposable baselines, confirming the stability of the fits and helping to validate the interpretation. For hydrodynamic size measurement, a small amount of CeO_2 powder was ground well with few drops of water, dispersed in water, stirred mechanically and ultrasonicated to produce a suspension. The pH of the CeO_2 suspension was raised above 10 for achieving a stable suspension (zeta potential greater than −35 mV). Size measurements for the cerium oxide nanocrystals in suspension were performed at 25 °C by photon correlation spectroscopy (PCS; this is also referred to as dynamic light scattering (DLS)) on a Zetasizer 3000 HSA, (Malvern, Worcestershire, U.K.) using a 60 mW He−Ne laser operating at a wavelength of 633 nm and at detection angle of 90°. The average hydrodynamic diameter was quantified using the *Z*-average size, based on the intensity of scattered light, obtained by cumulants analysis of the correlograms. This analysis also yields the polydispersity index (PDI): values below 0.3 are indicative of unimodal size distributions with smaller values demonstrating increasing monodispersity.

3. RESULTS AND DISCUSSION

Primary Sample Characterization. The recorded XRD patterns for four selected powder samples, synthesized through different techniques, are presented in Figure 1. The XRD

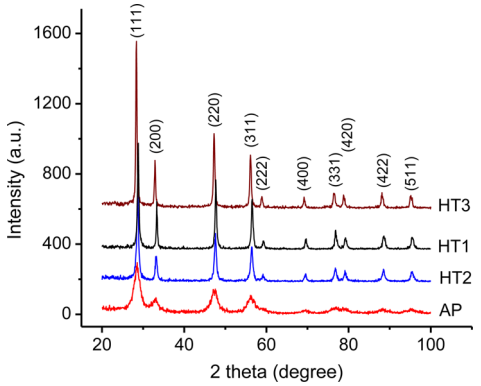

Figure 1. X-ray diffraction (XRD) patterns of CeO_2 powders AP, HT1, HT2, and HT3 synthesized through different routes. The patterns of HT3, HT2, and HT1 are scaled to avoid overlapping.

profiles for all the nanopowders match those of the fcc structure [space group: $Fm\bar{3}m$ (225)] of crystalline CeO_2 (JCPDS Card No. 34-394) with fluorite-type structure in which each metal cation is surrounded by eight O atoms.[37] The refinement of the lattice constants revealed small deviation in unit-cell parameters (lattice constant a = 0.541−0.545 nm) in CeO_2 of rod/tube shapes, as well as ammonia-precipitated crystals, indicative of small structural distortion due to crystal defects.[19] Thus, the XRD patterns reveal that the as-prepared ammonia-precipitated and hydrothermally treated powders are crystalline CeO_2.

There is moderate broadening of the diffraction peaks in AP, which suggests smaller crystals in this sample. The phase identity and purity of CeO_2 were confirmed by selected area electron diffraction, FT-IR spectroscopy and by X-ray photoelectron spectroscopy (see the Supporting Information). Thermogravimetry data demonstrate that the CeO_2 specimens are almost anhydrous. For instance, in the case of HT2 (Figure

DOI: 10.1021/acsami.5b00298
ACS Appl. Mater. Interfaces 2015, 7, 8545−8555

S5 in the Supporting Information), a total loss of ~8.6% was observed in three steps, upon heating up to 850 °C, with 4.8% being attributable to structural water. This suggests a stoichiometry of cerium oxide to crystallized water $CeO_2 \cdot 0.48H_2O$.

An important factor in developing new nanotechnologies for materials applications is the need to produce nanocomposites. In most preparative schemes, good dispersibility, preferably in aqueous suspension, is required. For this reason, we studied the colloidal properties of aqueous suspensions of AP and HT1 (as examples of both methods) by photon correlation spectroscopy (PCS). The average hydrodynamic size (D_{PCS}) for HT1 is 26 nm with a polydispersity index (PDI) of 0.19. For AP, D_{PCS} is 17 nm with a PDI of 0.26. The low PDI values indicate that the suspensions are relatively monodisperse. At pH ~10, the zeta potential of the suspensions was measured as −30 mV. The suspensions were stable for several days under these conditions, as one would expect, given the strong surface charge. This opens up possibilities for solution-based nanocompositing that we are currently investigating.

Electron Microscopy. A detailed morphological and structural analysis of the samples was undertaken using bright field high-resolution TEM; typical results are shown in Figure 2

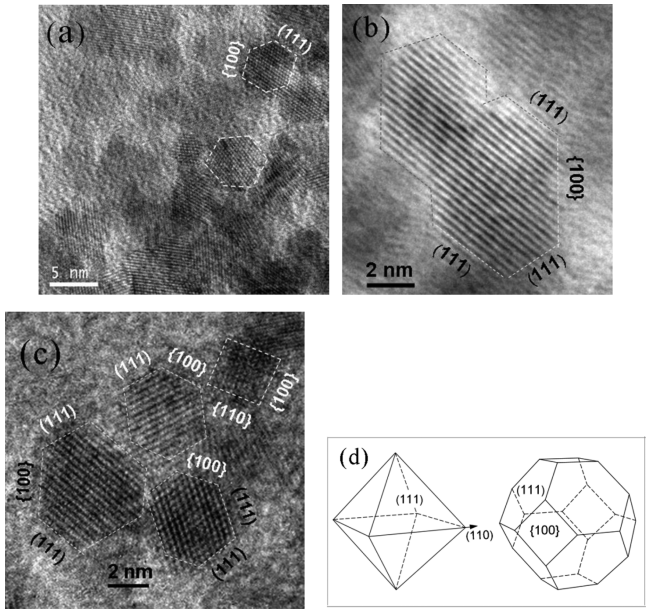

Figure 2. (a) Bright-field TEM images of ammonia-precipitated CeO_2 particles AP. Also shown are typical high-resolution TEM images of CeO_2 nanoparticles displaying (b) a coherent interface in AP and (c) the {100} and {111} facets of cubic CeO_2 (AP). (d) Schematic model showing the formation of a truncated octahedral from an octahedron.

and 3 (see Figures S3 and S4 in the Supporting Information for more TEM images). The ammonia-precipitated CeO_2 nanoparticles in AP are found to be almost spherical. The calculated mean particle size (D_{TEM}) on at least 50 particles from multiple TEM images in AP is 5.3 nm, with a standard deviation of σ = 0.99 nm (D_{XRD} = 5.2 nm), as shown in Figure 2a. Lattice fringes attributed to (111), (200), and (220) crystal planes with corresponding interplanar spacings of 0.31, 0.27, and 0.19 nm, respectively, which are characteristic of fcc CeO_2, were identified in HR-TEM images of spheroidal crystals in AP (Figure 2a). A careful examination reveals that the particles are dominated by {111} and {200} fringes along the [110]

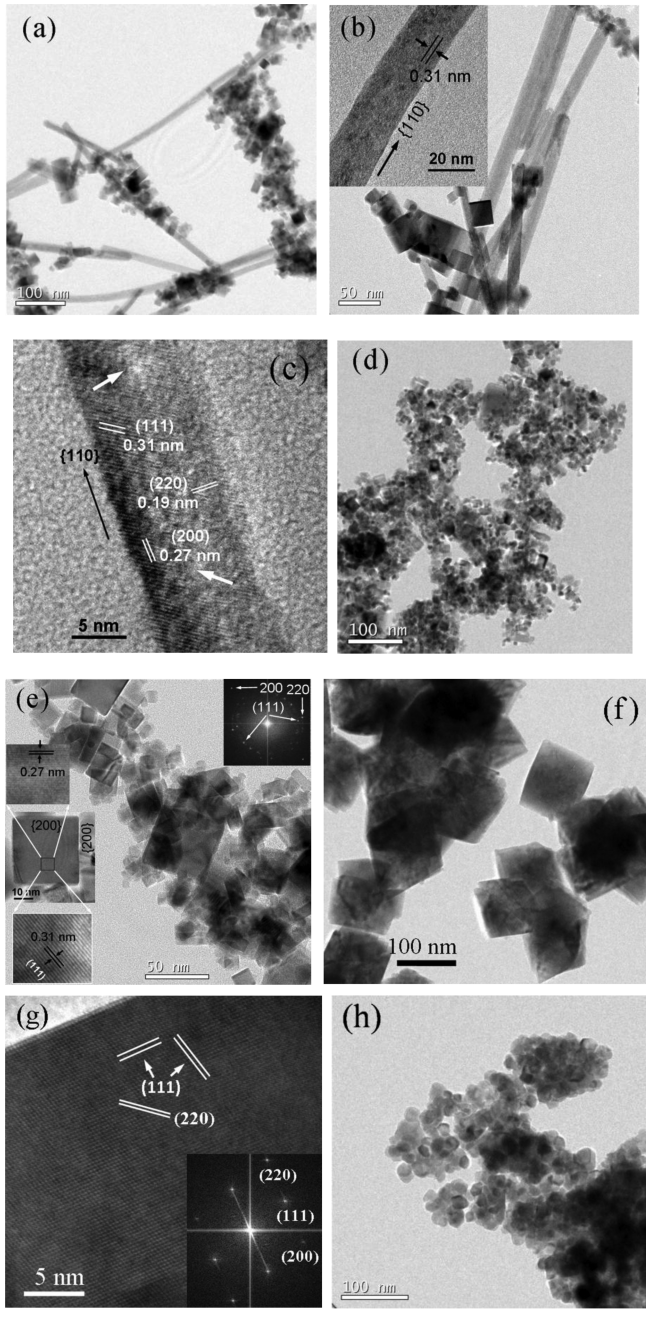

Figure 3. TEM image of hydrothermally synthesized CeO_2 crystals, (a,b) HT1 containing nanorods and cubes autoclaved at 120 °C. (c) HR-TEM image of a nanorod in HT1. (d,e) HR-TEM images of nanocubes in HT2 autoclaved at 180 °C; the insets at the bottom left in panel e shows nanocubes exhibiting (111) and {100} lattice planes, and the inset in the top right corner shows the fast Fourier transform (FFT) analysis. (f) HR-TEM image of HT3 comprising nano-octahedrons. (g) HR-TEM image of an octahedral particle (FFT analysis is shown as an inset). (h) TEM image of commercial ceria.

observation, establishing that the shape of the ceria nanocrystals is the truncated octahedral (polyhedra) enclosed by eight {111} and six {200} planes (Figure 2d), as reported by others.[38]

Crystal planes of same type tend to align with each other to minimize the interface strain,[39] forming a coherent interface (Figure 2b). High-resolution TEM micrographs of CeO_2 samples synthesized hydrothermally are shown in Figure 3. Mild hydrothermal treatment at 120 °C with a high base

DOI: 10.1021/acsami.5b00298
ACS Appl. Mater. Interfaces 2015, 7, 8545−8555

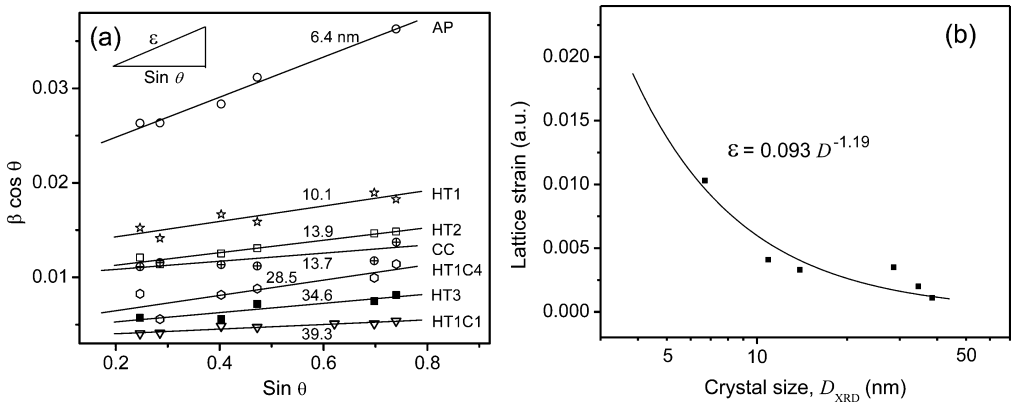

Figure 4. (a) Representative Williamson–Hall plots of β cos θ versus sin θ, for the reasonably well-resolved reflections (see Figure 1) of CeO_2 nanocrystals, synthesized by ammonia precipitation and hydrothermal methods: AP, HT1, HT2, CC, HT1C4, HT3, and HT1C1. The solid lines are linear regressions to the data. The crystal sizes, calculated from the intercepts, are also noted close to the respective fits in the figure. The crystal sizes, calculated from the intercepts, are also noted close to the respective fits in the figure. (b) Semilogarithmic plot of the variation in lattice strain with the size of CeO_2 crystals of different shapes; the solid line is a least-square fit of a power law to the data.

concentration (8 M) produced predominantly nanorods (HT1) from anisotropic growth of unstable $Ce(OH)_3$ nuclei, governed by a dissolution recrystallization mechanism. When the autoclave temperature was increased to 180 °C (HT2), nanocubes with an average size (as determined via TEM) of D_{TEM} = 13.5 ± 2.5 nm were formed. Hydrothermal treatment of CN at 170 °C in the presence of a mineralizer $Na_3PO_4{\cdot}6H_2O$ resulted in the formation of perfect octahedral morphology (HT3) with sharp corners and well-defined edges. The octahedral particles are almost uniform in edge length of 80 ± 5 nm (Figure 3f). TEM analysis of sample HT1 demonstrates that it consists of a mixture of cubic and rod-shaped crystals of CeO_2.

Detailed analysis of multiple images (e.g., Figure 3a,b) reveals that it contains ∼31.5% nanorods (number) with an average length of ∼355 nm and a diameter of ∼22 nm. This equates to an average (equivalent sphere) diameter of ∼60 nm. The remaining 68.5% are nanocubes with an average edge length of ∼18.4 nm. By volume (or mass), the sample is ∼91% rods and ∼9% cubes (see the Supporting Information). The square faces of the CeO_2 nanocubes are enclosed by {100} planes. The strong presence of {111} facets is evidenced by fast Fourier transform (FFT) analysis (see the inset to Figure 3e). The (111) crystal facets pass diagonally across the surface of the cubes (see insets of Figure 3e). One-dimensional (1D) growth is seen in the HR-TEM images of nanorods in the {110} direction with {111} as well as {100} exposed surfaces. FFT analysis of Figure 3c confirmed the presence of {111} and {110} facets only. By contrast, Yang et al. reported growth along the [211] direction.[40] Point defects due to missing atoms or local deformation due to the twist of parallel planes are observed on the nanorod surfaces in some instances, these are marked by arrowheads in Figure 3c. The prevalence of such defects will lead to enhance the catalytic performance. The HR-TEM image in conjunction with FFT analysis in Figure 3f and 3g reveals that the octahedral particles are enclosed by eight {111} planes (see the Supporting Information for more images). Once we reduced the hydrothermal treatment temperature in the synthesis of HT1 from 120 to 100 °C, we observed the same mixed morphology in which the extent of cubes is reduced below 5% by volume (see Figure S3 in the Supporting Information).

Detailed X-ray Diffraction Analysis. The mean crystal diameter and microstrain of the CeO_2 nanocrystals were evaluated by line-profiling of prominent XRD peaks. In the Williamson–Hall approach, the peak width, β, is expressed as

$$\beta \cos \theta = 2\varepsilon \sin \theta + \frac{0.9\lambda}{D} \quad (1)$$

where ε is the lattice microstrain and β is calculated from the relation

$$\beta = \frac{\sum I{\cdot}I}{I_{max}} \quad (2)$$

where $\sum I{\cdot}I$ represents the integrated peak intensity of the X-ray feature, and I_{max} is the observed maximum intensity. By plotting the β cos θ against sin θ for several XRD peaks at different 2θ values, the average crystal size (D_{XRD}) and strain (ε) are determined from the intercept and the slope of the linear regression to the data, respectively. Crystallite size is often determined from XRD profile using the Scherrer equation;[41,42] however, this underestimates grain size, since it ignores broadening of the diffraction peaks, because of microstrain in the lattice,[14] so it is not appropriate for this study. Williamson–Hall plots for all the nanocrystalline CeO_2 powders and the dependence of lattice strain in CeO_2 nanocrystals of different shapes and sizes with crystal diameter (D_{XRD}) are shown in Figure 4. The D_{XRD} values are provided in Table 1. As indicated in the figure, the strain data conforms very well to a single power law, even for samples prepared in very different ways. The value for the power, 1.19, is in the range reported by other workers.[15] The strain values in the range of 0.0041–0.0011, obtained for HT1, HT2, and HT1C1, are much smaller than those previously reported for CeO_2 crystals of comparable sizes, which were synthesized by wet chemical methods.[15,36] Interestingly, the lattice strain of 0.0041 in HT1 is further reduced to 0.0011 in HT1C1, upon calcination at 1000 °C.

Evidently, the extended duration (∼24 h) used in the hydrothermal treatment, and subsequent calcinations, results in larger crystallites with reduced microstrain.[43] On the basis of previous experiments, this difference is expected to affect the catalytic activity of the surfaces;[15] indeed, the catalytic activity for this sample did change drastically (see below).

DOI: 10.1021/acsami.5b00298
ACS Appl. Mater. Interfaces 2015, 7, 8545–8555

Table 1. Primary Physical Characterization of the CeO_2 Nanocrystal Samples

sample[a]	morphology	D_{XRD} [nm]	D_{TEM} [nm]	D_{BET} [nm]	specific surface area [$m^2\ g^{-1}$]	lattice parameter [nm]
AP	spheres	6.4	6	5.8	143	0.544
HT1	cubes and rods	10.1	60[b]	12.5	66	0.542
HT2	cubes	13.9	13.5	19.7	42	0.542
HT3	octahedra	34.6	80[c]	137.9	6	0.541
HT1C4	large cubes and rods	28.5	nd[d]	36.9	22.4	0.541
CC	spheres and cubes	13.7	20	165	5	0.543
HT1C1	large cubes and rods	39.3		nd[d]	<1	0.541

[a]AP = ammonia-precipitated spherical ceria NPs; HT1 and HT2 are hydrothermally synthesized ceria at 120 and 180 °C; CC = commercial ceria. HT3 is synthesized at a temperature of 170 °C. HT1C4 and HT1C1 are HT1 calcined at 400 and 1000 °C. [b]Equivalent sphere diameter (see text). [c]Average edge length of octahedra. [d]The BET equivalent size could not be measured for this sample, given the low SSA.

Harris analysis was also performed on the CeO_2 XRD data.[33,44] The preferred orientation of the crystallographic planes was estimated and expressed as the texture coefficient $C(h_ik_il_i)$, following the equation

$$C(h_ik_il_i) = \frac{I(h_ik_il_i)}{I_0(h_ik_il_i)}\left[\frac{1}{n}\sum\frac{I(h_ik_il_i)}{I_0(h_ik_il_i)}\right]^{-1} \quad (3)$$

where $I(h_ik_il_i)$ is the diffraction intensity of the $(h_ik_il_i)$ plane of the particular sample under investigation, $I_0(h_ik_il_i)$ is the intensity of the $(h_ik_il_i)$ plane from the standard JCPDS powder diffraction pattern for the corresponding peak i, and n is the number of reflections taken into account. A sample with randomly oriented crystallites presents a $C(hkl)$ of 1, while a larger value indicates an abundance of crystallites oriented to that (hkl) plane.[32]

The $C(hkl)$ for the seven CeO_2 specimens of this study and of commercial CeO_2 (CC) are shown in Figure 5. Preferential orientation of the crystallites along the higher energy planes {100} was apparent in most cases, but particularly for the hydrothermally synthesized samples. However, calcining HT1 at 400 and 1000 °C (HT1C4 and HT1C1), has resulted in preferential growth of CeO_2 crystals in stable, low energy {111} facets, a feature that is common to the commercial product (CC).

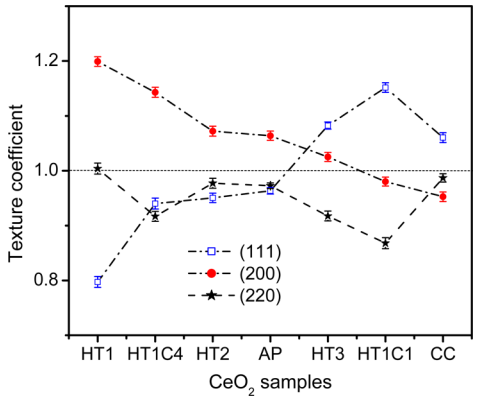

Figure 5. Texture coefficient of CeO_2 nanocrystals of different shapes calculated from their powder X-ray diffraction (XRD) patterns (reference JCPDS File Card No. 34-394). The error bars represent the standard deviation estimated on the basis of the three independent measurements.

XPS and Raman Spectral Analysis. Because of the lower energy requirement for the interconversion between the two oxidation states (1.72 eV), the Ce^{3+} state exists to some extent, along with the Ce^{4+} in CeO_2.[45] For the detailed study of $[Ce^{3+}]$/oxygen vacancies in the system, the XPS and Raman spectra of selected samples were analyzed. Figure 6 shows the XPS survey and Ce 3d spectra of HT1 (see Figure S2 in the Supporting Information for more XPS spectra).

The XPS wide spectrum shows the peaks attributed to the core levels of Ce 4d, Ce 3d, O 1s, and C 1s where the Ce 3d electron core level is characterized by $3d_{5/2}$ and $3d_{3/2}$ series peaks.[46] In the Ce 3d spectrum, v_0, v_1, u_0, and u_1 peaks are attributed to Ce^{3+}; v, v'', v''', u, u'', and u''' are the characteristic peaks of Ce^{4+} ions. The concentrations of Ce^{3+} in all the products were estimated using the integrated area of each peak in the spectrum, the values are given in Table S1 in the Supporting Information. The Ce^{3+} content was found to be 44.3%, 35.5%, and 26.2% in samples HT1, HT2 and AP, respectively (Table S1 in the Supporting Information). The Ce 3d spectrum of commercial ceria could not be resolved as it contains impurities (dopant cations; see Figure S2 in the Supporting Information). The Ce^{3+} concentration in HT1 (rod−cube) is almost twice the same contained in AP (spheres) and is slightly higher than that reported for 2 nm CeO_2 nanodots in our earlier work,[46] substantiating the size and shape dependence of Ce^{3+} content. It is known that the presence of Ce^{3+} in the fluorite lattice, generates oxygen vacancies to maintain charge balance.[47,48] The presence of surface oxygen vacancies in the materials was monitored by ultraviolet (UV)−Raman spectroscopy (see Figure 7), which shows the presence of peaks at 460 (γ peak), 560 (α peak), and 600 cm^{-1} (β peak), respectively. A small peak characteristic of $O_2^{\delta-}$ ($0 < \delta < 1$) species was observed at ~1340 cm^{-1} in all the samples. The main peak at ca. 460 cm^{-1} is due to the F_{2g} mode vibration of cubic fluorite structure in CeO_2.[49]

The phonon modes at 560 and 600 cm^{-1} are characteristic of oxygen vacancies in the ceria system.[46,47,49] Following the observation made by Wu et al., the relative density of defect sites (~560 cm^{-1}) in nanoparticulate CeO_2 varies as HT1 (rod−cube) > HT2 (nanocubes) ≥ AP (nanopolyhedra) > HT3 (octahedra).[50] CeO_2 possess a high oxygen storage capacity (OSC), because of the rapid formation and elimination of oxygen vacancy defects in it. The higher Ce^{3+} concentration ensuing in defects and exposure of more reactive {100} surfaces, followed by {110} surfaces, can facilitate the formation of oxygen vacancies in them[10,12] and introduce enhanced oxygen storage capacity in the material, as shown in Table 2. We note that the OSC, as determined by thermogravimetry,[47] increases in the order HT1 > HT2 > AP > HT3 > CC. The highest value obtained was 420.6 μmol g^{-1} O_2 for HT1 (rod−cube), which possesses the highest concentration of Ce^{3+} (44.3%), and reactive polar {100} surfaces. An exact comparison with reported literature seems to be meaningless as the method of OSC calculation is very sensitive to the experimental conditions, and the values may change drastically with change in the experimental conditions. Still it is interesting to note that the value of OSC for mixed morphology was

DOI: 10.1021/acsami.5b00298
ACS Appl. Mater. Interfaces 2015, 7, 8545−8555

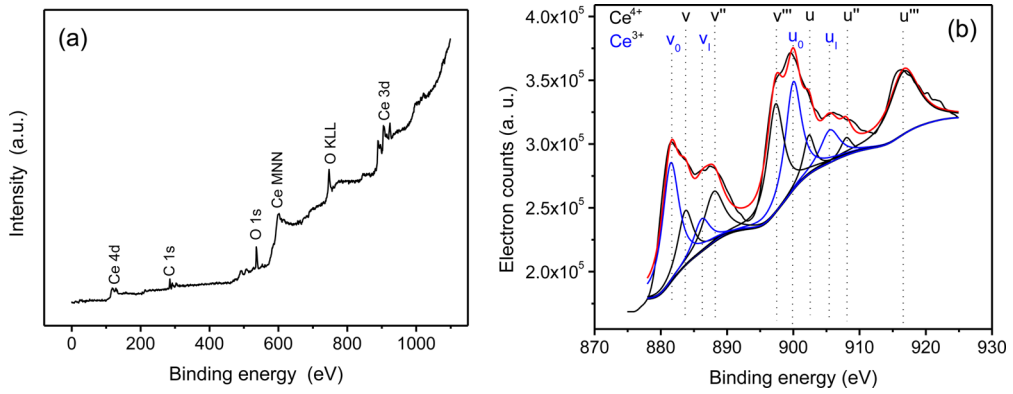

Figure 6. XPS pattern of HT1 (a) survey spectrum and (b) deconvoluted Ce 3d core level.

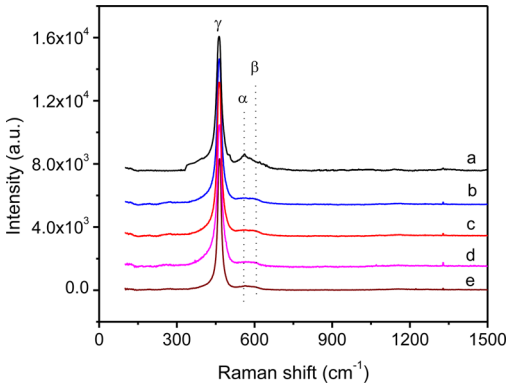

Figure 7. Raman spectra of HT1 (spectrum a), HT2 (spectrum b), AP (spectrum c), CC (spectrum d), and HT3 (spectrum e) at 633 nm excitation taken at room temperature.

Table 2. Oxygen Storage Capacity and [Ce^{3+}] from Deconvoluted Ce 3d XPS Spectra

sample	wt loss [%]	oxygen vacancy content, δ	total OSC [μmol O g^{-1}]	Ce^{3+} [%]
HT1	1.346	0.431	420.6	44.3
HT2	0.76	0.287	280.9	35.4
HT3	0.4921	0.157	153.8	
AP	0.8988	0.243	237.5	26.2
CC	0.3147	0.1	98.3	nd[a]

[a]Not determined. [Ce^{3+}] could not be calculated as the Ce 3d spectrum of commercial ceria is not well resolved (see Figure S2c in the Supporting Information).

between that reported for pure rods and cubes by Mai et al. The reported OSC value is 554 and 353 μmol O_2 g^{-1} for pure ceria nanorods and nanocubes, respectively.[12]

Overview of Physical Properties. Selected data from the range of characterization techniques are presented in Table 1. It is clear that both the D_{XRD} and D_{BET} values (which are statistical averages of the entire sample) are in excellent numerical agreement with D_{TEM} (which is evaluated from a limited number of micrographs) for samples AP and HT2. This validates our choice of the Williamson−Hall procedure for measuring D_{XRD} and strengthens the validity of the strain values obtained. It also confirms that particles in samples AP and HT2 are single crystals, as is suggested by the observation of sharp parallel crystal facets in the HR-TEM micrographs. It is generally found that the macroscopic surface area of the samples shows the expected correlation with NP size, the hydrothermally synthesized samples having SSA values almost an order of magnitude lower that those produced by precipitation. For sample HT1, widely differing average size and crystal diameter ($D_{TEM} \approx 60$ nm and $D_{XRD} = 10.1$ nm) are observed, because this sample is composed of a mixture of nanocubes and nanorods. It is very interesting that, despite this difference, the dependence of crystal strain on D_{XRD} for this sample (Figure 4B) perfectly matches the behavior of the single-crystalline powders. The hydrodynamic diameter (D_{PCS}) for AP was 17 nm (PDI = 0.26), indicating the presence of small clusters of crystals.[51] However, in the case of HT1, D_{PCS} was only 26 nm (PDI = 0.19). This demonstrates that the larger nanorods are not dispersible and the suspension produced from HT1 is composed of dispersed nanocubes, with an edge length of ~18.4 nm (from TEM), given that the D_{PCS} value is the average based on the light scattering intensity, which is proportional to the sixth power of particle size. At the detection angle used in this study (90°), the experiment is particularly sensitive to the presence of any aggregates. Hence, for this suspension, the number of clusters of nanocubes, if any, must be very small. This approach based on preferential precipitation is currently under investigation in our laboratory with a view to isolate the isotropic and anisotropic fractions as pure materials.

Thus, in summary, precipitation produces samples composed of single spherical crystals of CeO_2 <7 nm in size, with a slight preponderance of high energy {100} facets. The hydrothermal approach produces materials composed of nanocubes or mixtures of rods and cubes. This mixture can be separated if required. The crystals in the hydrothermally produced samples have a greater preponderance of high-energy {100} facets than in the powders prepared by precipitation. Thermal treatment of the samples produced by the hydrothermal approach results in a significant increase in crystal size, and these are now dominated by less active {111} facets. So that approach may be disadvantageous for practical applications.

Catalytic Activity. The catalytic activity of the CeO_2 powders was evaluated by measuring the peak combustion temperature (T_P) and the total heat evolved (ΔH) during the CeO_2 catalyzed combustion of carbonaceous materials (diesel soot) in excess O_2. The carbonaceous soot was characterized by TGA which revealed a total combustibles content of 92.50 wt % and the presence of 6.75 wt % moisture. Hence, the remaining 0.75% is neither volatile nor combustible. In Figure 8, these results are presented as a function of the sum of the texture coefficients (C) of the active planes (200) and (220) of CeO_2. The figure shows that catalytic activity, in terms of the total

DOI: 10.1021/acsami.5b00298
ACS Appl. Mater. Interfaces 2015, 7, 8545−8555

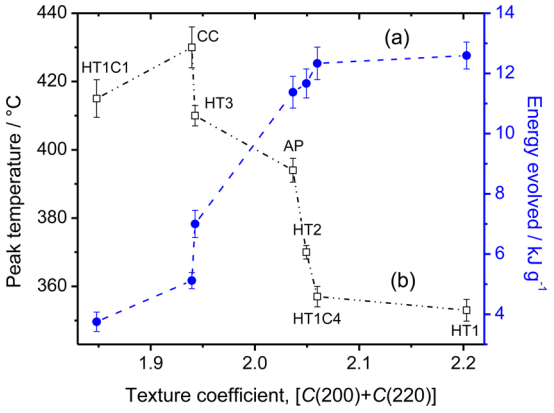

Figure 8. Variation of (a) energy evolved and (b) peak temperature against [C(200) + C(220)], which shows the catalytic activity of ceria nanoparticles. Reading from the left the samples are HT1C1 (SSA < 1 m^2 g^{-1}), CC (SSA = 5 m^2 g^{-1}), HT3 (SSA = 6 m^2 g^{-1}), AP (SSA = 143 m^2 g^{-1}), HT2 (SSA = 42.2 m^2 g^{-1}), HT1C4 (SSA = 22.4 m^2 g^{-1}), and HT1 (SSA = 66 m^2 g^{-1}).

heat evolved from the soot combustion, varies from a minimum of 4 kJ g^{-1}, for HT1C1, to a maximum of 13.0 kJ g^{-1}, for HT1. These values are in the expected range: 15 kJ g^{-1} has been reported for coal.[31] The same samples define the range of peak combustion temperatures (T_P) in this study, which were generally inversely correlated with the total heat evolved; the extreme values were 430 and 353 °C for CC and HT1, respectively.

The T_P value for uncatalyzed soot oxidation was 518 °C; hence, HT1 could reduce the soot oxidation temperature by ∼165 °C. We noted above (Figure 5) that the texture coefficients vary from sample to sample. We now note (Table 3) that the sum of texture coefficients for the facets (200) and

Table 3. Crystal Dimensions and Texture Coefficients of Different Crystal Facets of CeO_2

sample	D_{XRD} [nm]	C[111]	C[200]	C[220]	C[200] + C[220]
HT1	10.1	0.7972	1.199	1.004	2.203
HT1C4	28.5	0.9401	1.1429	0.9169	2.0598
HT2	13.9	0.9505	1.0721	0.9772	2.0493
AP	6.4	0.9634	1.0638	0.9727	2.0365
HT3	34.6	1.0823	1.0251	0.9175	1.9426
CC	13.7	1.0604	0.9526	0.9869	1.9395
HT1C1	39.3	1.1516	0.9802	0.868	1.8482

(220) [C(200) + C(220)] increases in the order HT1 > HT1C4 > HT2 > AP > HT3 > HT1C1 > CC, which are considered to be more active, is a minimum (1.85) in HT1C1 and maximum (2.20) in HT1. The soot combustion temperature of various nanocatalysts decreases in the order CC > HT1C1 > HT3 > AP > HT2 > HT1C4 > HT1. It should be noted that the catalytic activity measurements were performed in triplicate and, for each sample, at least two independent preparations were completed. The error bars represent the standard deviation estimated on the basis of the three measurements.

Hence, the measurements show significant variation in activity from sample to sample that is not correlated with the SSA of the powders (Table 1). The SSA of the highly active HT1 was in the range reported by other authors.[12,25,48] It is also interesting to note that the reduction in T_P (32%) was better than that reported by Fino et al. (30%) for self-assembled ceria stars with a high SSA of 105 m^2 g^{-1}.[22] Palmisano et al. have reported ∼27% reduction in soot oxidation temperature in the presence of 8 nm ceria NPs prepared by a solution combustion method.[31] By comparison, despite the very low SSA of 1 m^2 g^{-1}, HT1C1 shows ∼20% reduction in T_P. Lopez et al. reported a reduction in soot combustion temperature of ∼7% and 26% with CeO_2 and $Ce_{0.69}Zr_{0.31}O_2$, respectively.[52] The effect of rare-earth-doped ceria in soot oxidation has been studied by Makkee et al., who reported ∼24% reduction in soot combustion temperature with 10 mol % La-doped ceria calcined at 1000 °C.[53] Ravishankar et al. studied Pt/CeO_2 nanohybrids in CO oxidation with a rod-shaped ceria support and reported ∼21% and 31% reduction in the light-off temperature, with respect to that of cubical and octahedral nanoparticles, respectively.[21] An increase in the number of contact points between soot and catalyst was suggested as a significant contributor to enhanced activity.[22,31] By comparison, we observed slightly higher (∼32%) reduction in T_P using HT1 which contains ∼9% CeO_2 nanorods. However, most reports instead refer to the high availability of surface oxygen and high surface reducibility of ceria by virtue of its morphology or in the presence of suitable dopants.[21,25,52,53] Our study suggests that the peak temperature and energy evolved from a ceria-catalyzed combustion reaction are largely dependent on the energetics of the surface, as expressed in this study by texture coefficient.

Considering the energy evolved during soot oxidation, we find that, except for CC, the trend in ΔH is not associated with formation method, surface area, or crystal size, but once again with the sum of the texture coefficients of the active planes C(200) and C(220). We tentatively attribute the deviation of T_P in CC to factors related to the presence of dopant metal ions. This reaffirms that the exposed {100} and {110} facets exhibit greater catalytic activity, compared to {111} facets.[19] As expected, the peak combustion temperature (T_P) is found to broadly follow the opposite trend; more efficient catalysis is associated with a higher energy generation at lower temperature. Comparing the hydrothermal to the precipitation approaches, we find that, generally, for the HT series, greater C(200) values and lower C(220) are observed. However, the trend in activity is only apparent when the sum of the texture coefficients is examined. So once again, the soot combustion study reaffirms our findings from the OSC measurements. This suggests that the activity is shared across these crystal facets, irrespective of the method of synthesis, crystal size, or morphology. It is interesting to note that, for both the HT and AP series, increasing the Ce concentration resulted in increased activity (as indicated by ΔH and T_P). Given the preceding discussion, we tentatively attribute this to a marginal increase in C(220). In HT1C1, which is produced by annealing HT1 at 1000 °C, we observe only a minor reduction in catalytic activity due to crystal growth (D_{XRD} ≈ 39 nm) preferentially in the least active (111) plane, as indicated by a decrease in C(200) and an increase in C(111). It is interesting and assuring to note that HT1 retained its morphology and catalytic activity in soot oxidation even after heating the CeO_2 at 400 °C (HT1C4) and 1000 °C (HT1C1; see Figure S3 in the Supporting Information) and is far better than commercial ceria powder, as evidenced by the soot combustion temperatures of 357 and 415 °C, respectively, with respect to the same at 430 °C with CC.

Sample HT1 is unusual in that it contains a mixture of nanorods and nanocubes, the latter of which comprising ∼9%

DOI: 10.1021/acsami.5b00298
ACS Appl. Mater. Interfaces 2015, 7, 8545−8555

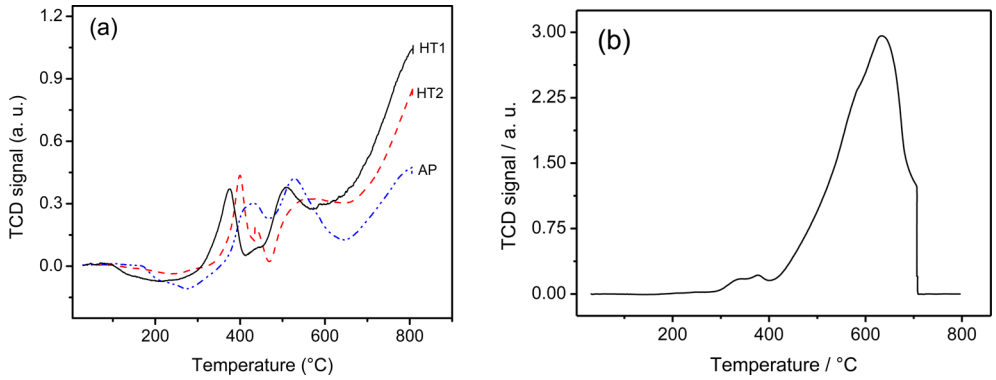

Figure 9. H_2-TPR profiles of (a) HT1, HT2, and AP, and (b) commercial CeO_2.

of the sample by mass. The fraction of the total surface area corresponding to the cubes is therefore <1%, and they are predominantly bound with {100} facets. Therefore, the sample activity arises almost exclusively due to the nanorods and the ΔH value for HT1 follows the trend of the other samples. To further confirm the role of nanocubes in the mixed morphology, a sample containing <5 vol % of cubes prepared hydrothermally at 100 °C (see the Supporting Information) was also tested for catalytic activity. The T_P value was found to increase from 353 °C to 357 °C, the variation being only 1.1%. However, the T_P value for HT1 is lower than that for the other samples. This suggests different reaction kinetics for the exposed {100} and {110} facets that dominate the surfaces of the rods, which are far more extended in this case. Once again, there is no strict correlation between the SSA and the peak temperature, indicating that the energetics on the surface are the defining factor determining the combustion behavior.

H_2-TPR profiles of selected powders compiled in Figure 9 provide further information on enhanced catalytic activity of our CeO_2 samples, compared to that of commercial ceria. The reduction profiles show two broad maxima and a further reduction maximum; the former features, observed at 650 °C, are attributed to a global process corresponding to the consumption of surface oxygen species, whereas the maxima at ∼800 °C arise from bulk reduction. In the commercial CeO_2 sample, the bulk peak is only observed, which is reasonable, taking into account that the BET surface area of this sample is very low (5 m^2 g^{-1}). Bulk oxygen must be transported to the surface before reduction, and, consequently, the bulk reduction takes place at temperatures higher than that of surface reduction.[54] The peak characteristic of surface oxygen species appears at 373, 400, and 431 °C in HT1, HT2, and AP, respectively, indicating that the synthesized nanomaterials possess relatively stronger surface activity. During the soot oxidation, the function of the catalyst is to increase the "active oxygen" transfer to the soot surface.[55] Clusters of more than two vacancies, such as linear surface oxygen vacancies known to be present in mixed morphology catalysts, are favorable for the migration of oxygen.[48]

The increased surface oxygen vacancies in our materials, as evidenced by the XPS and Raman analyses, enhance the surface oxygen mobility and activity, although as noted earlier, the defining influence of the relative preponderance of active facets dominates. In the case of commercial ceria, as a large amount of lattice oxygen is released at high temperature by this catalyst the T_P value of 353 °C in HT1 increases to 430 °C. The surface reduction temperatures from the H_2-TPR profiles follow the same order of activity for the CeO_2 samples, as is observed in soot oxidation (Figure 8), which reconfirms the involvement of the active crystal facets in catalysis/chemical reactions. We can conclude that the activity of a cerium oxide material was not limited by the available surface but by the energetics of the reaction on the exposed crystal facets in all cases.

4. CONCLUSIONS

Nanocrystalline CeO_2 have been synthesized using a simple one-step, surfactant-free, precipitation technique and by hydrothermal methods. Despite the differences in crystal shape and size that result, the lattice strain was found to follow a single scaling law with strain decreasing nonlinearly with increases in the average crystal size. It was also found that the adoption of crystals with higher {100} facets produced enhanced catalytic activity. The highest Ce^{3+} concentration of ∼44% in mixed morphology catalyst, which was responsible for the high OSC, contributed to the enhanced catalytic activity. A remarkable feature which makes the mixed morphology catalyst a promising candidate for soot oxidation is that they retain catalytic activity even after thermal aging at a temperature as high as 1000 °C. The study demonstrates, for the first time, that engineered exposed crystal facets with low strain have high activity, and therefore places understanding of the activity on a stronger physical basis. We anticipate that this will enable the production of both CeO_2 and oxide nanocomposite catalysts, which have been gaining wider attention in recent years.

■ ASSOCIATED CONTENT

Supporting Information

The detailed experimental procedure adopted for oxygen storage capacity measurement, FT-IR, TGA, XPS, and HR-TEM images of ceria nanocatalysts. This material is available free of charge via the Internet at http://pubs.acs.org.

■ AUTHOR INFORMATION

Corresponding Author

*Tel.: +91-33-23223546. Fax: +91-33-24730957. E-mail: swapankumar.ghosh2@mail.dcu.ie.

Notes

The authors declare no competing financial interest.

■ ACKNOWLEDGMENTS

The authors are grateful to the Director, National Institute for Interdisciplinary Science & Technology (NIIST), CSIR, for providing the necessary facilities for the work and CSIR-Central Glass & Ceramic Research Institute for continuing the same.

DOI: 10.1021/acsami.5b00298
ACS Appl. Mater. Interfaces 2015, 7, 8545−8555

We thank Dept. of Science & Technology (DST) and CSIR, India for providing HR-TEM facility to NIIST. MMD (X-ray), HR-TEM staffs are kindly acknowledged for their assistance in obtaining XRD and electron microscopy data. This work was partly funded by the Indian Rare Earths Limited Technology Development Council (IRELTDC), DAE, India.

REFERENCES

(1) Si, R.; Zhang, Y. W.; You, L. P.; Yan, C. H. Rare-Earth Oxide Nanopolyhedra, Nanoplates, and Nanodisks. *Angew. Chem., Int. Ed.* **2005**, *44*, 3256−3260.
(2) Si, R.; Zhang, Y. W.; You, L. P.; Yan, C. H. Self-Organized Monolayer of Nanosized Ceria Colloids Stabilized by Poly-(Vinylpyrrolidone). *J. Phys. Chem. B* **2006**, *110*, 5994−6000.
(3) Bondioli, F.; Corradi, A. B.; Leonelli, C.; Manfredini, T. Nanosized CeO_2 Powders Obtained by Flux Method. *Mater. Res. Bull.* **1999**, *34*, 2159−2166.
(4) Fernandez-Garcia, M.; Martinez-Arias, A.; Hanson, J. C.; Rodriguez, J. A. Nanostructured Oxides in Chemistry: Characterization and Properties. *Chem. Rev.* **2004**, *104*, 4063−4104.
(5) Sreeremya, T. S.; Krishnan, A.; Iyengar, S. J.; Ghosh, S. Ultra-Thin Cerium Oxide Nanostructures Through a Facile Aqueous Synthetic Strategy. *Ceram. Int.* **2012**, *38*, 3023−3028.
(6) Sreeremya, T. S.; Krishnan, A.; Mohamed, Peer; Hareesh, U. S.; Ghosh, S. Synthesis and Characterization of Cerium Oxide Based Nanofluids: An Efficient Coolant in Heat Transport Applications. *Chem. Eng. J.* **2014**, *255*, 282−289.
(7) Atkinson, A.; Barnett, S.; Gorte, R. J.; Irvine, J. T. S.; McEvoy, A. J.; Mogensen, M.; Singhal, S. C.; Vohs, J. Advanced Anodes for High-Temperature Fuel Cells. *Nat. Mater.* **2004**, *3*, 17−27.
(8) Murugan, B.; Ramaswamy, A. V. Defect-Site Promoted Surface Reorganization in Nanocrystalline Ceria for the Low-Temperature Activation of Ethylbenzene. *J. Am. Chem. Soc.* **2007**, *129*, 3062−3063.
(9) Sreeremya, T. S.; Thulasi, K. M.; Krishnan, A.; Ghosh, S. A Novel Aqueous Route to Fabricate Ultrasmall Monodisperse Lipophilic Cerium Oxide Nanoparticles. *Ind. Eng. Chem. Res.* **2012**, *51*, 318−326.
(10) Deori, K.; Gupta, D.; Saha, B.; Awasthi, S. K.; Deka, S. Introducing Nanocrystalline CeO_2 as Heterogeneous Environmental Friendly Catalyst for the Aerobic Oxidation of Para-xylene to Terephthalic Acid in Water. *J. Mater. Chem. A* **2013**, *1*, 7091−7099.
(11) Schulz, H.; Stark, W. J.; Maciejewski, M.; Pratsinis, S. E.; Baiker, A. Flame-Made Nanocrystalline Ceria/Zirconia Doped with Alumina or Silica: Structural Properties and Enhanced Oxygen Exchange Capacity. *J. Mater. Chem.* **2003**, *13*, 2979−2984.
(12) Mai, H. X.; Sun, L. D.; Zhang, Y. W.; Si, R.; Feng, W.; Zhang, H. P.; Liu, H. C.; Yan, C. H. Shape-Selective Synthesis and Oxygen Storage Behavior of Ceria Nanopolyhedra, Nanorods, and Nanocubes. *J. Phys. Chem. B* **2005**, *109*, 24380−24385.
(13) Jun, Y. W.; Choi, J. S.; Cheon, J. Shape Control of Semiconductor and Metal Oxide Nanocrystals Through Non-hydrolytic Colloidal Routes. *Angew. Chem., Int. Ed.* **2006**, *45*, 3414−3439.
(14) Tjong, S. C.; Chen, H. Nanocrystalline Materials and Coatings. *Mater. Sci. Eng.* **2004**, *45*, 1−88.
(15) Deshpande, S.; Patil, S.; Kuchibhatla, S.; Seal, S. Size Dependency Variation in Lattice Parameter and Valency States in Nanocrystalline Cerium Oxide. *Appl. Phys. Lett.* **2005**, *87*, 133113.
(16) Hsiao, W. I.; Lin, Y. S.; Chen, Y. C.; Lee, C. S. The Effect of the Morphology of Nanocrystalline CeO_2 on Ethanol Reforming. *Chem. Phys. Lett.* **2007**, *441*, 294−299.
(17) Huang, W. Crystal Plane-Dependent Surface Reactivity and Catalytic Property of Oxide Catalysts Studied with Oxide Nanocrystal Model Catalysts. *Top. Catal.* **2013**, *56*, 1363−1376.
(18) Zhou, K. B.; Wang, X.; Sun, X. M.; Peng, Q.; Li, Y. D. Enhanced Catalytic Activity of Ceria Nanorods from Well-Defined Reactive Crystal Planes. *J. Catal.* **2005**, *229*, 206−212.
(19) Chen, W. T.; Chen, K. B.; Wang, M. F.; Weng, S. F.; Lee, C. S.; Lin, M. C. Enhanced Catalytic Activity of $Ce_{1-x}M_xO_2$ (M = Ti, Zr, and Hf) Solid Solution with Controlled Morphologies. *Chem. Commun.* **2010**, *46*, 3286−3288.
(20) Guan, Y. J.; Hensen, E. J. M.; Liu, Y.; Zhang, H. D.; Feng, Z. C.; Li, C. Template-Free Synthesis of Sphere, Rod and Prism Morphologies of CeO_2 Oxidation Catalysts. *Catal. Lett.* **2010**, *137*, 28−34.
(21) Singhania, N.; Anumol, E. A.; Ravishankar, N.; Madras, G. Influence of CeO_2 morphology on the catalytic activity of CeO_2-Pt hybrids for CO oxidation. *Dalton Trans.* **2013**, *42*, 15343−15354.
(22) Miceli, P.; Bensaid, S.; Russo, N.; Fino, D. CeO_2 Based Catalysts with Engineered Morphologies for Soot Oxidation to Enhance Soot-Catalyst Contact. *Nanoscale Res. Lett.* **2014**, *9*, 254.
(23) Yang, S. W.; Gao, L. Controlled Synthesis and Self-Assembly of CeO_2 Nanocubes. *J. Am. Chem. Soc.* **2006**, *128*, 9330−9331.
(24) Nolan, M.; Parker, S. C.; Watson, G. W. The Electronic Structure of Oxygen Vacancy Defects at the Low Index Surfaces of Ceria. *Surf. Sci.* **2005**, *595*, 223−232.
(25) Gao, Y.; Wang, W.; Chang, S.; Huang, W. Morphology Effect of CeO_2 Support in the Preparation, Metal-Support Interaction, and Catalytic Performance of Pt/CeO_2 Catalysts. *ChemCatChem.* **2013**, *5*, 3610−3620.
(26) Qiao, Z. A.; Wu, Z.; Dai, S. Shape-Controlled Ceria-Based Nanostructures for Catalysis Applications. *ChemSusChem* **2013**, *6*, 1821−1833.
(27) Deori, K.; Gupta, D.; Saha, B.; Deka, S. Design of 3-Dimensionally Self-Assembled CeO2 Nanocube as a Breakthrough Catalyst for Efficient Alkylarene Oxidation in Water. *ACS Catal.* **2014**, *4*, 3169−3179.
(28) Conesa, J. C. Surface Anion Vacancies on Ceria: Quantum Modelling of Mutual Interactions and Oxygen Adsorption. *Catal. Today* **2009**, *143*, 315−325.
(29) Huang, H. H.; Chang, H. P.; Chien, Y. T.; Huang, M. C.; Wang, J. S. Influence of Annealing Temperature on the Grain Growth of Samarium-Doped Ceria. *J. Cryst. Growth* **2006**, *287*, 458−462.
(30) Zhao, P.; Ito, A.; Tu, R.; Goto, T. Preparation of Highly (100)-Oriented CeO_2 Films on Polycrystalline Al_2O_3 Substrates by Laser Chemical Vapor Deposition. *Surf. Coat. Technol.* **2010**, *204*, 3619−3622.
(31) Palmisano, P.; Russo, N.; Fino, P.; Fino, D.; Badini, C. High Catalytic Activity of SCS Synthesized Ceria Towards Diesel Soot Combustion. *Appl. Catal., B* **2006**, *69*, 85−92.
(32) Navaladian, S.; Viswanathan, B.; Varadarajan, T. K.; Viswanath, R. P. A Rapid Synthesis of Oriented Palladium Nanoparticles by UV Irradiation. *Nanoscale Res. Lett.* **2009**, *4*, 181−186.
(33) Harris, G. B. Quantitative Measurement of Preferred Orientation in Rolled Uranium Bars. *Philos. Mag.* **1952**, *43*, 113−123.
(34) Zhou, X. D.; Huebner, W.; Anderson, H. U. Processing of Nanometer-Scale CeO_2 Particles. *Chem. Mater.* **2003**, *15*, 378−382.
(35) Yan, L.; Yu, R. B.; Chen, J.; Xing, X. R. Template-Free Hydrothermal Synthesis of CeO_2 Nano-octahedrons and Nanorods: Investigation of the Morphology Evolution. *Cryst. Growth Des.* **2008**, *8*, 1474−1477.
(36) Dutta, P.; Pal, S.; Seehra, M. S.; Shi, Y.; Eyring, E. M.; Ernst, R. D. Concentration of Ce^{3+} and Oxygen Vacancies in Cerium Oxide Nanoparticles. *Chem. Mater.* **2006**, *18*, 5144−5146.
(37) Taniguchi, T.; Watanabe, T.; Sakamoto, N.; Matsushita, N.; Yoshimura, M. Aqueous Route to Size-Controlled and Doped Organophilic Ceria Nanocrystals. *Cryst. Growth Des.* **2008**, *8*, 3725−3730.
(38) Zhang, J.; Ohara, S.; Umetsu, M.; Naka, T.; Hatakeyama, Y.; Adschiri, T. Colloidal Ceria Nanocrystals: A Tailor-Made Crystal Morphology in Supercritical Water. *Adv. Mater.* **2007**, *19*, 203−306.
(39) Wang, Z. L.; Feng, X. D. Polyhedral Shapes of CeO_2 Nanoparticles. *J. Phys. Chem. B* **2003**, *107*, 13563−13566.
(40) Du, N.; Zhang, H.; Chen, B. G.; Ma, X. Y.; Yang, D. R. Ligand-Free Self-Assembly of Ceria Nanocrystals into Nanorods by Oriented Attachment at Low Temperature. *J. Phys. Chem. C* **2007**, *111*, 12677−12680.

DOI: 10.1021/acsami.5b00298
ACS Appl. Mater. Interfaces 2015, 7, 8545−8555

(41) Hu, C. G.; Zhang, Z. W.; Liu, H.; Gao, P. X.; Wang, Z. L. Direct Synthesis and Structure Characterization of Ultrafine CeO_2 Nanoparticles. *Nanotechnology* **2006**, *17*, 5983−5987.
(42) Leoni, M.; Scardi, P. Nanocrystalline Domain Size Distributions from Powder Diffraction Data. *J. Appl. Crystallogr.* **2004**, *37*, 629−634.
(43) Rupp, J. L. M.; Infortuna, A.; Gauckler, L. J. Microstrain and Self-Limited Grain Growth in Nanocrystalline Ceria Ceramics. *Acta Mater.* **2006**, *54*, 1721−1730.
(44) Ramgir, N. S.; Mulla, I. S.; Vijayamohanan, K. P. Effect of RuO_2 in the Shape Selectivity of Submicron-Sized SnO_2 Structures. *J. Phys. Chem. B* **2005**, *109*, 12297−12303.
(45) Jaimy, K. B.; Safeena, V. P.; Ghosh, S.; Hebalkar, N. Y.; Warrier, K. G. K. Photocatalytic Activity Enhancement in Doped Titanium Dioxide by Crystal Defects. *Dalton Trans.* **2012**, *41*, 4824−4832.
(46) Krishnan, A.; Sreeremya, T. S.; Murray, E.; Ghosh, S. One-Pot Synthesis of Ultra-Small Cerium Oxide Nanodots Exhibiting Multi-Colored Fluorescence. *J. Colloid Interface Sci.* **2013**, *389*, 16−22.
(47) Bharali, P.; Saikia, P.; Reddy, B. M. Large-Scale Synthesis of Ceria-Based Nano-oxides with High CO Oxidation Activity. *Catal. Sci. Technol.* **2012**, *2*, 931−933.
(48) Liu, X.; Zhou, K.; Wang, L.; Wang, B.; Li, Y. Oxygen Vacancy Clusters Promoting Reducibility and Activity of Ceria Nanorods. *J. Am. Chem. Soc.* **2009**, *131*, 3140−3141.
(49) Taniguchi, T.; Sonoda, Y.; Echikawa, M.; Watanabe, Y.; Hatakeyama, K.; Ida, S.; Koinuma, M.; Matsumoto, Y. Intense Photoluminescence from Ceria-Based Nanoscale Lamellar Hybrid. *ACS Appl. Mater. Interfaces* **2012**, *4*, 1010−1015.
(50) Wu, Z.; Li, M.; Howe, J.; Meyer, H. M.; Overbury, S. H. Probing Defect Sites on CeO_2 Nanocrystals with Well-Defined Surface Planes by Raman Spectroscopy and O_2 Adsorption. *Langmuir* **2010**, *26*, 16595−16606.
(51) Ghosh, S.; Divya, D.; Remani, K. C.; Sreeremya, T. S. Growth of Monodisperse Nanocrystals of Cerium Oxide During Synthesis and Annealing. *J. Nanopart. Res.* **2010**, *12*, 1905−1911.
(52) Atribak, I.; Bueno-Lopez, A.; Garcia-Garcia, A. Thermally Stable Ceria−Zirconia Catalysts for Soot Oxidation by O_2. *Catal. Commun.* **2008**, *9*, 250−255.
(53) Krishna, K.; Bueno-Lopez, A.; Makkee, M.; Moulijn, J. A. Potential Rare Earth Modified CeO_2 Catalysts for Soot Oxidation I. Characterisation and Catalytic Activity with O_2. *Appl. Catal., B* **2007**, *75*, 189−200.
(54) Ranga Rao, G.; Mishra, B. G. Structural, Redox and Catalytic Chemistry of Ceria Based Materials. *Bull. Catal. Soc. India* **2003**, *2*, 122−134.
(55) Meher, S. K.; Ranga Rao, G. Novel Nanostructured CeO_2 as Efficient Catalyst for Energy and Environmental Applications. *J. Chem. Sci.* **2014**, *26*, 361−372.

DOI: 10.1021/acsami.5b00298
ACS Appl. Mater. Interfaces 2015, 7, 8545−8555